Rotationally resolved PFI-ZEKE photoelectron spectroscopic study of the low-lying electronic states of ArXe#

Author(s):
Piticco, Lorena; Merkt, Frédéric

Publication date:
2012-09-07

Permanent link:
https://doi.org/10.3929/ethz-a-010780483

Originally published in:
The Journal of Chemical Physics 137(9), https://doi.org/10.1063/1.4747549

Funding acknowledgement:
135342 - Rydberg states, VUV laser spectroscopy and photoionization dynamics (SNF)

The following article appeared in *J. Chem. Phys.* **137**, 094308 (2012) and may be found at http://dx.doi.org/10.1063/1.4747549.

Rotationally resolved PFI-ZEKE photoelectron spectroscopic study of the low-lying electronic states of ArXe+

Lorena Piticco and Frédéric Merkt

Citation: The Journal of Chemical Physics **137**, 094308 (2012); doi: 10.1063/1.4747549
View online: http://dx.doi.org/10.1063/1.4747549
View Table of Contents: http://scitation.aip.org/content/aip/journal/jcp/137/9?ver=pdfcov
Published by the AIP Publishing

Rotationally resolved PFI-ZEKE photoelectron spectroscopic study of the low-lying electronic states of $ArXe^+$

Lorena Piticco and Frédéric Merkt[a)]
Laboratorium für Physikalische Chemie, ETH Zürich, 8093 Zürich, Switzerland

(Received 28 June 2012; accepted 8 August 2012; published online 6 September 2012)

Rotationally resolved pulsed-field-ionization zero-kinetic-energy photoelectron spectra of the X 1/2, A_1 3/2, and A_2 1/2 electronic states of the $ArXe^+$ molecular ion have been recorded following resonant (1+1′) two-photon excitation via selected rovibrational levels of the C 1 and D 0^+ states of selected isotopomers of the ArXe molecule. Using rovibronic selection and propensity rules for the photoionization out of these intermediate molecular states enabled the determination of the parity of the molecular-ion levels and of the magnitude and sign of the Ω-doubling constants of the coupled X 1/2 ($p \approx 4B$) and A_2 1/2 ($p \approx -2B$) states of $ArXe^+$. The results indicate that these molecular-ion states can be approximately described using Mulliken's second variant of Hund's angular momentum coupling case (c), for which J_a, the total electronic and spin angular momentum of the two atoms, is a good quantum number (semi-united atom). The analysis of the rotational structure enabled the derivation of improved values of the dissociation energies, equilibrium distances, and molecular constants for the X 1/2, A_1 3/2, and A_2 1/2 states of $ArXe^+$. © *2012 American Institute of Physics*. [http://dx.doi.org/10.1063/1.4747549]

I. INTRODUCTION

The heteronuclear rare-gas dimer ions Rg–Rg′$^+$ (Rg, Rg′ = Ne, Ar, Kr, Xe, and Rn) possess six low-lying electronic states which correspond to the four valence-shell configurations $(\sigma)^2(\pi)^4(\pi^*)^4(\sigma^*)^1$, $(\sigma)^2(\pi)^4(\pi^*)^3(\sigma^*)^2$, $(\sigma)^2(\pi)^3(\pi^*)^4(\sigma^*)^2$, and $(\sigma)^1(\pi)^4(\pi^*)^4(\sigma^*)^2$. These states are either labeled using Hund's case (a) and (b) nomenclature as A $^2\Sigma_{1/2}$, B $^2\Pi_\Omega$ (Ω = 1/2, 3/2), C $^2\Pi_\Omega$ (Ω = 1/2, 3/2), and D $^2\Sigma_{1/2}$,[1–3] or using Hund's case (c) nomenclature as X 1/2, A_1 3/2, A_2 1/2, B 1/2, C_1 3/2, and C_2 1/2.[4–8] The two labelling schemes use the same letters (A, B, and C) for different states, and the correspondence between the two labelling schemes is X 1/2 ↔ A $^2\Sigma^+_{1/2}$, A_1 3/2 ↔ B $^2\Pi_{3/2}$, A_2 1/2 ↔ B $^2\Pi_{1/2}$, B 1/2 ↔ D $^2\Sigma^+_{1/2}$, C_1 3/2 ↔ C $^2\Pi_{3/2}$, and C_2 1/2 ↔ C $^2\Pi_{1/2}$.

At large internuclear separation, these states asymptotically approach one of the four dissociation limits (I) Rg′$^+$ ($^2P_{3/2}$) + Rg($^1S_0$), (II) Rg′$^+$ ($^2P_{1/2}$) + Rg($^1S_0$), (III) Rg′($^1S_0$) + Rg^+ ($^2P_{3/2}$), and (IV) Rg′($^1S_0$) + Rg^+ ($^2P_{1/2}$). Choosing Rg and Rg′ to be the lighter and heavier of the two rare-gas atoms, respectively, ensures that these dissociation limits are numbered in order of increasing energy. Two states (X 1/2 and A_1 3/2) are associated with the first dissociation limit, one (A_2 1/2) with the second, two (B_1 1/2 and C_1 3/2) with the third, and one (C_2 1/2) with the fourth.

The molecular orbital diagram and the Born-Oppenheimer potential-energy functions of the six low-lying electronic states of $ArXe^+$ are depicted in panels (a) and (b) of Figure 1 to illustrate their general behavior and the correlation from the region of short internuclear separation, where the states are usually labeled using the Hund's case (a) and (b) nomenclature mentioned above, to the region of large internuclear separation, where the states are more conveniently designated using Hund's case (c) labels. In this latter region, the interaction between the two atoms becomes so weak that the electron orbital motion is no longer coupled to the internuclear axis and Λ ceases to be a good quantum number. The A $^2\Sigma_{1/2}$ and B $^2\Pi_{1/2}$ states are strongly mixed by the spin-orbit interaction in this region, and so are the C $^2\Pi_{1/2}$ and D $^2\Sigma_{1/2}$ states, whereas the B $^2\Pi_{3/2}$ and C $^2\Pi_{3/2}$ retain their Hund's case (a) $^2\Pi_{3/2}$ character. At large internuclear distances, the positive charge is localized on one of the rare-gas atoms, but, at short range, the charge is partially transferred to the other atom so that the Σ states are of mixed A $^2\Sigma$ and D $^2\Sigma$ character and the Π states of mixed B $^2\Pi$ and C $^2\Pi$ character.[7,9–11]

The rare-gas dimer ions are prototypical systems to study charge-transfer processes in the presence of spin-orbit interactions.[12,13] The knowledge of their potential-energy functions and spectroscopic properties is also relevant to understanding the electronic spectrum of the neutral rare-gas dimers.[14–17] Indeed, all electronically excited states of the rare-gas dimers have Rydberg character and may be regarded, in first approximation, as a rare-gas dimer ion weakly interacting with a Rydberg electron.

The spectroscopic information available on the rare-gas dimer ion $ArXe^+$, which is the object of the present investigation, consists of vibrationally resolved spectra of the C_2 1/2 → X 1/2, B 1/2 → X 1/2, C_1 3/2 → A_1 3/2, C_2 1/2 → A_2 1/2, and B 1/2 → A_2 1/2 band systems,[6,8] photoionization spectra,[18] photoelectron spectra (PES) following resonance-enhanced multiphoton excitation,[2] threshold photoelectron-photoion coincidence spectra,[19,20] and pulsed-field-ionization zero-kinetic-energy (PFI-ZEKE) photoelectron spectra[9] recorded following resonant 1+1′ two-photon

a)Electronic mail: merkt@xuv.phys.chem.ethz.ch.

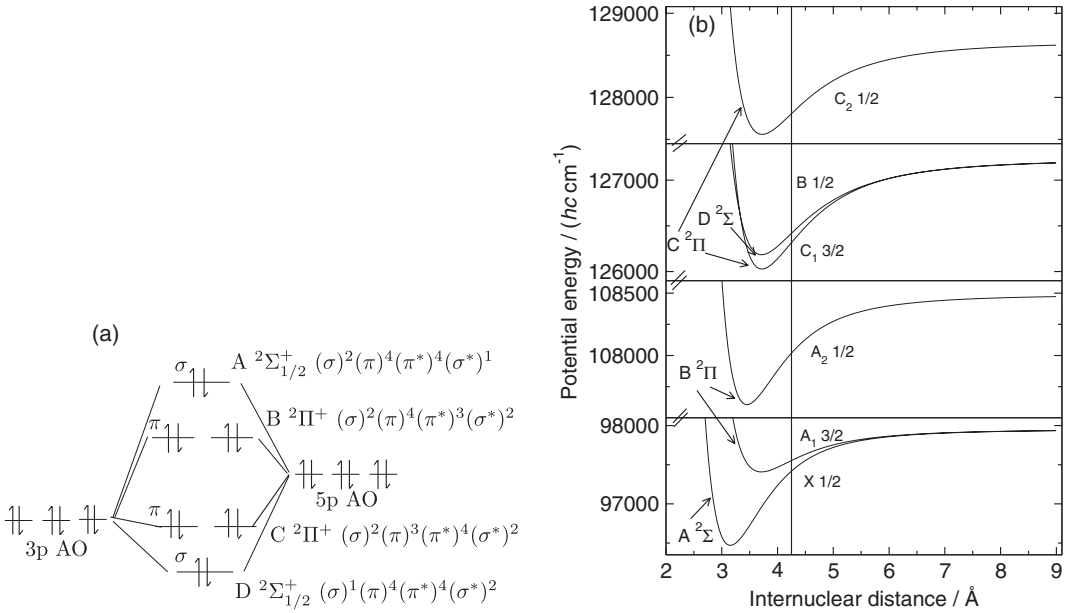

FIG. 1. (a) Schematic molecular orbital diagram of ArXe arising from the 3*p* and 5*p* atomic valence orbitals of Ar and Xe, respectively. The electronic configurations and Hund's case (a) and (b) labels of the low-lying electronic states of $ArXe^+$ one obtains by removing one electron from each of the molecular orbitals are indicated on the right-hand side. (b) Potential-energy functions of the six low-lying electronic states of $ArXe^+$. The vertical line marks the equilibrium internuclear separation in the X 0^+ neutral ground state. Adapted from Ref. 9.

excitation. From the determination of isotopic shifts in the PFI-ZEKE photoelectron spectra of several isotopomers, absolute vibrational assignments of the X 1/2 ← X, A_1 3/2 ← X, and A_2 1/2 ← X photoelectron bands of ArXe could be derived.[6,9,20] A global analysis of the high-resolution spectroscopic data mentioned above led to the derivation of the potential-energy functions of all six low-lying states of $ArXe^+$ (Ref. 9) using a potential model adapted from the earlier work of Hausamann and Morgner.[7] The potential model indicates that the electronic states associated with the $Xe^+ + Ar$ and $Xe + Ar^+$ dissociation limits are mixed at short range and that it is necessary to consider charge-exchange interactions to accurately describe the measured vibronic energies of $ArXe^+$. Recently, Viehland *et al.*[21] have calculated the potential-energy functions of several heteronuclear rare-gas dimer cations *ab initio* and compared them with the potential-energy functions derived from experimental data. Although the overall agreement was reported to be satisfactory in the case of $ArXe^+$, Viehland *et al.* also pointed at several discrepancies, primarily concerning the dissociation energies, and to a lesser extent also the equilibrium internuclear distances, and questioned the reliability of the experimental data.

The goals of the investigation presented in this article were to obtain spectroscopic information on $ArXe^+$ at a resolution sufficiently high to observe the rotational structure of the low-lying electronic states of $ArXe^+$, and to check the validity of the earlier experimental results. These goals were achieved by recording PFI-ZEKE photoelectron spectra of ArXe using a $1+1'$ resonant two-photon excitation sequence via selected rovibrational levels of the C 1 and D 0^+ states. The narrow bandwidth of the vacuum ultraviolet (VUV) laser used to access the C and D states from the X ground neutral state also permitted us to select specific isotopomers, which turned out to be essential to reduce the spectral congestion of the PFI-ZEKE photoelectron spectra.

Resolving the rotational structure of the photoelectron spectra did not only enable the determination of the structural parameters, but it also contributed, with the help of rovibronic selection rules, to (i) obtain information on the dominant electronic configurations of the intermediate C 1 and D 0^+ states of ArXe, (ii) determine the parity of the rovibronic levels, and (iii) extract information on the Λ (Ω) doubling and the spin-rotation splittings of the coupled $^2\Pi_{1/2}$ and $^2\Sigma^+$ states.

II. GENERAL CONSIDERATIONS

A. The C 1 and D 0^+ electronic states of ArXe

The C 1 and D 0^+ states of ArXe are located in the vicinity of the $Xe(5p)^5 6s'[1/2]_1 + Ar(^1S_0)$ dissociation limit in the region between 77050 cm^{-1} and 77250 cm^{-1} above the X 0^+ ground state. These states can be classified as Rydberg states but are subject to strong configurational mixing.[22,23] Their rovibrational energy level structure has been measured at high resolution by $1_{VUV} + 1'$ resonance-enhanced two-photon ionization.[24,25] The *e*-symmetry levels of the C 1 and D 0^+ states are not predissociative and have lifetimes on the order of ~1 ns or more. The *f*-symmetry levels of the C 1 state are predissociative and their lifetimes decrease with increasing rotational excitation.

The $n = 6\ell\lambda$[ion core, Ω^+] Rydberg character of the configurations contributing to the C 1 and D 0^+ states of $ArXe^+$ can be exploited to derive propensity rules for photoionization. Indeed, photoionization from these intermediate levels can be assumed, in first approximation, not to change the ion-core character. Ion-core-preserving ionization channels are

TABLE I. Expected ionization channels in the single-photon threshold ionization from the C and D states of ArXe as estimated from the photoionization and PFI-ZEKE photoelectron spectra reported in Ref. 9.

State	Character	Ionization channel	Dominant partial waves	Mechanism
C 1	$6p\sigma$[A_1 3/2] strong	A_1 3/2 strong	s/d	Direct
	$6s\sigma$[A_2 1/2] strong	A_2 1/2 strong	p	Direct
	$6p\sigma/\pi$[X 1/2] weak	X 1/2 weak	s/d	Direct (weak)
				Indirect[a]
D 0^+	$6s\sigma$[A_2 1/2] strong	A_2 1/2 strong	p	Direct
	$6p\pi$[A_1 3/2] weak	A_1 3/2 weak	s/d	Direct + indirect[b]
	$6p\sigma$[X 1/2] very weak	X 1/2 very weak		Indirect[c]

[a]Channel interaction with A_1 3/2.
[b]Channel interaction with A_2 1/2.
[c]Channel interaction with A_2 1/2 and A_1 3/2.

thus predicted to be dominant, and ion-core changing ionization processes result from electronic autoionization.

The D 0^+ state possesses a regular rovibronic energy level structure[9,24,25] and is thought to have a dominant $6s\sigma$[A_2 1/2] character with weaker $6p\pi$[A_1 3/2] and possibly also $6p\sigma$[X 1/2] contributions. Single-photon ionization from the D 0^+ state therefore provides efficient direct access to the A_2 1/2 and A_1 3/2 states of $ArXe^+$ (see Figure 5 of Ref. 9) and indirect access to the X 1/2 state mediated by interactions between the X 1/2, A_1 3/2, and A_2 1/2 ionization channels.

The C 1 state has a strongly perturbed vibrational structure and can be described as a superposition of dominant $6p\sigma$[A_1 3/2], $6s\sigma$[A_2 1/2] and weaker $6p\sigma$[X 1/2] contributions.[22,25] The irregular vibrational structure of the C 1 state could be accounted for semiquantitatively by a two-state adiabatic coupling model involving the $6p\sigma$[A_1 3/2] and $6s\sigma$[A_2 1/2] states.[25] Single-photon ionization from the C 1 state does not only provide efficient direct access to the A_1 3/2 and A_2 1/2 states but also weaker access to the X 1/2 state of $ArXe^+$ (see Figure 5 of Ref. 9). Neither the C nor the D state have significant character of Rydberg states with a B_1, C_1, or C_2 ion core and, therefore, these ionic states are not easily accessible by single-photon excitation from the C and D states.[9] The investigation presented in this article focuses on the X 1/2, A_1 3/2, and A_2 1/2 states of $ArXe^+$.

Table I summarizes these considerations and lists the expected dominant ionization channels in the single-photon ionization of the C 1 and D 0^+ states of ArXe based on the simplifying assumptions that (i) the character of the ion core does not change upon ionization, and (ii) the dominant partial waves correspond to the atomic $\Delta l = \pm 1$ transition selection rules.

B. Photoionization selection rules, Λ (Ω) doublings and spin-rotation splittings in the coupled $^2\Sigma$ and $^2\Pi$ states of $ArXe^+$

The $^2\Sigma^+$ and $^2\Pi$ low-lying electronic states of the rare-gas dimer ions are coupled by the spin-orbit interaction, which leads to large spin-rotation splittings of the levels of the $^2\Sigma^+$ states and large Λ (or Ω) doublings of the $^2\Pi_{1/2}$ states.[26,27] The analysis of the rotational structures of these states can either be performed using expressions derived from effective Hamiltonians adapted to Hund's case (c) angular momentum coupling[26–28]

$$E_{\Omega=1/2}(v^+, J^+)/hc = T_{1/2}^{(v^+)} + B_{1/2}^{(v^+)}\left[J^+(J^+ + 1) - \frac{1}{2}\right] \pm (-1)^{(J^+-(1/2))} P^{(v^+)}\left(J^+ + \frac{1}{2}\right), \quad (1)$$

$$E_{\Omega=3/2}(v^+, J^+)/hc = T_{3/2}^{(v^+)} + B_{3/2}^{(v^+)}\left[J^+(J^+ + 1) - \frac{9}{2}\right], \quad (2)$$

or using expressions describing the coupling between $^2\Sigma_{1/2}^+$ and $^2\Pi$ states[29]

$$E(^2\Sigma^+; v^+, N^+, F_1)/hc = T_{\Lambda=0}^{(v^+)} + B_{\Lambda=0}^{(v^+)} N^+(N^+ + 1) + \frac{1}{2}\gamma^{(v^+)} N^+, \quad \text{for } J^+ = N^+ + 1/2, \quad (3)$$

$$E(^2\Sigma^+; v^+, N^+, F_2)/hc = T_{\Lambda=0}^{(v^+)} + B_{\Lambda=0}^{(v^+)} N^+(N^+ + 1) - \frac{1}{2}\gamma^{(v^+)}(N^+ + 1), \quad \text{for } J^+ = N^+ - 1/2, \quad (4)$$

$$E(^2\Pi_{1/2}; v^+, J^+, e)/hc = T_{1/2}^{(v^+)} + B_{1/2}^{(v^+)}\left[J^+(J^+ + 1) + \frac{1}{4}\right] + \frac{1}{2}p^{(v^+)}(J^+ + 1/2), \quad (5)$$

$$E(^2\Pi_{1/2}; v^+, J^+, f)/hc = T_{1/2}^{(v^+)} + B_{1/2}^{(v^+)}\left[J^+(J^+ + 1) + \frac{1}{4}\right] - \frac{1}{2}p^{(v^+)}(J^+ + 1/2). \quad (6)$$

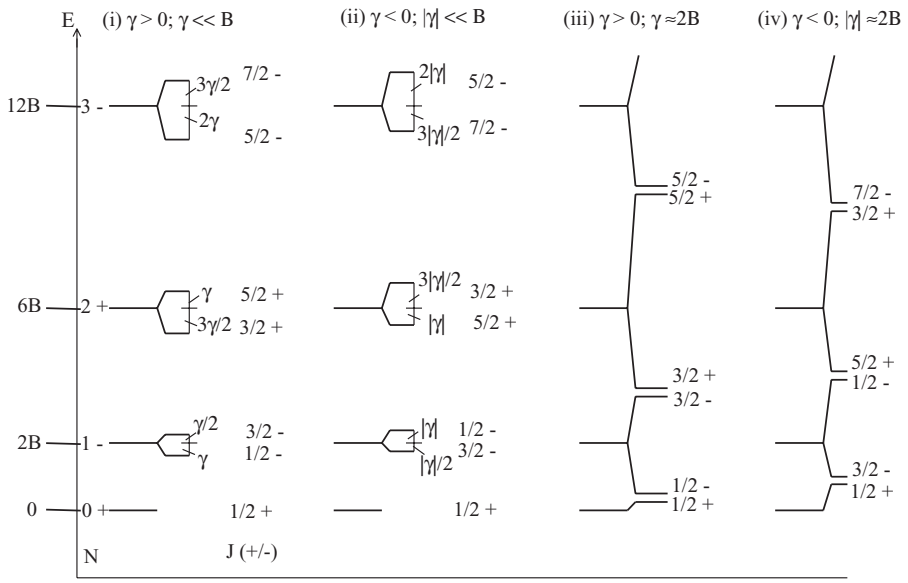

FIG. 2. Generic patterns showing the rovibrational energy level structure of $^2\Sigma^+$ states for (i) $\gamma > 0$, $\gamma \ll B$; (ii) $\gamma < 0$, $|\gamma| \ll B$; (iii) $\gamma > 0$, $\gamma \approx 2B$; and (iv) $\gamma < 0$, $|\gamma| \approx 2B$.

The expressions (1)–(6) only list the terms that are relevant at the resolution of ≈ 0.1 cm^{-1} of our experiments. The $^2\Sigma^+ - {}^2\Pi$ interaction (spin-orbit and L-uncoupling) manifests itself primarily in the values of the spin-rotation $\gamma^{(v^+)}$ and Λ-doubling $p^{(v^+)}$ parameters. The spectral patterns of the $^2\Sigma^+$ and $^2\Pi$ states critically depend on the magnitude and sign of these constants and can be classified in four generic patterns depicted in Figures 2 and 3 for $^2\Sigma^+$ and $^2\Pi$ states, respectively (see also discussion in Ref. 26).

In all four patterns of Figure 2, the levels group in pairs (doublets). For $|\gamma| \ll B$, the levels form pairs that have the same parity. Depending on the sign of γ, the components with the larger J values are either the upper ones (pattern (i)) or the lower ones (pattern (ii)). For $|\gamma| \approx 2B$, the components of the doublets have opposite parity (patterns (iii) and (iv)) and have either the same J value (pattern (iii)) or J values differing by 2 (pattern (iv)).

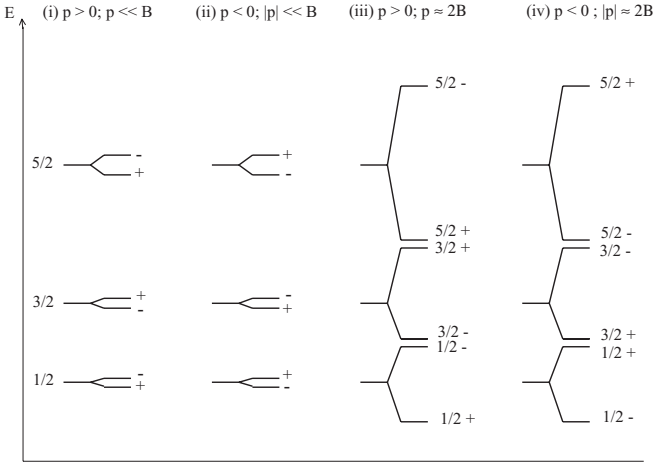

FIG. 3. Generic patterns showing the rovibrational energy level structure of $^2\Pi$ states for (i) $p > 0$, $p \ll B$; (ii) $p < 0$, $|p| \ll B$; (iii) $p > 0$, $p \approx 2B$; and (iv) $p < 0$; $|p| \approx 2B$.

In the case of the $^2\Pi$ state, the levels also group in pairs (see Fig. 3). At low values of $|p|$, the pairs consist of levels of the same J value but of opposite parity (patterns (i) and (ii)) and differ in the energetic order of the two parity components. For $|p| \approx 2B$, the patterns consist of pairs of levels of the same parity and J values differing by one (patterns (iii) and (iv)). In the special case $|\gamma| \approx B$ and $|p| \approx B$, which corresponds to a pure Hund's case (c) situation, the level structure is regular, without pairing of the levels (see Figure 1 of Ref. 26). Assigning the rotational structure of a photoelectron spectrum to one of the patterns in Figures 2 and 3 represents a challenge and is only possible if the observed intensity patterns can unambiguously be interpreted on the basis of photoionization selection or propensity rules.

The general photoionization selection rules for diatomic molecules relevant for the analysis are[30]

$$\Delta J = J^+ - J = -l - 3/2, -l - 1/2, \ldots, l + 3/2, \quad (7)$$

and

$$\begin{aligned} &+ \leftrightarrow +, - \leftrightarrow -, + \not\leftrightarrow - \text{ for } l \text{ odd}, \\ &+ \leftrightarrow -, + \not\leftrightarrow +, - \not\leftrightarrow - \text{ for } l \text{ even}, \end{aligned} \quad (8)$$

and depend on the magnitude and even/odd nature of the orbital angular momentum quantum number l of the photoelectron partial wave. In Eq. (7), J^+ and J represent, respectively, the total angular momentum quantum number (excluding nuclear spin) of the cationic state, and of the neutral state out of which the electron is ejected. The $\pm 3/2$ and $\pm 1/2$ contributions on the right-hand side of Eq. (7) result from the vector addition of the spin of the photoelectron ($s = 1/2$) and of the photon orbital angular momentum ($l = 1$ in the electric-dipole approximation). Equation (8) results from the $+ \leftrightarrow -$ nature of electric-dipole transitions and from the even/odd parity of even/odd-l partial waves. A single-center expansion of the molecular orbital out of which the electron is ejected in combination with the Laporte rule $\Delta l = l - l_o = \pm 1$ for

photoexcitation (l_o is the angular momentum quantum number of the components of the single-center expansion) often enables qualitatively correct predictions of the dominant partial waves.[31–33] When ionization occurs out of a Rydberg state of well defined l_o value, the prediction of the partial waves is straightforward (see Table I), although rovibronic interactions between the different ionization channels can significantly affect the intensity distributions[34,35] and the noncentrosymmetric structure of ArXe inevitably mixes orbital components of different l_o values and partial waves of different l values (e.g., *s-p* mixing). Indeed, when the center of mass is not located at the center of an atom, the character of the molecular orbital differs from that of the atomic orbital and can be estimated from an origin-shift transformation.

III. EXPERIMENT

The experiments were carried out using the method of PFI-ZEKE photoelectron spectroscopy. The ionization-threshold region was reached from the X 0^+ neutral state in a resonant $1_{VUV} + 1'$ two-photon excitation sequence via selected rovibrational levels of either the D 0^+ or the C 1 intermediate state. Because of the small value of the rotational constant of $ArXe^+$ (typically < 0.05 cm^{-1}), the rotational structure of the photoelectron spectra could only be resolved when a single rotational level of a single isotopomer was selected in the intermediate level.

The laser system and photoelectron spectrometer employed to obtain the data presented in this article have been described in Refs. 25 and 36, respectively. The narrow-bandwidth VUV laser (bandwidth 0.01 cm^{-1}) used to select individual rovibrational levels of the C 1 and D 0^+ states is the same as that used in our study of the C-X and D-X band systems of ArXe.[25] The laser used to access the region of the ionization thresholds from the selected intermediate level was a commercial dye laser (Radiant dyes, Narrow Scan) with a bandwidth of 0.1 cm^{-1}. The multipulse electric-field ionization sequences used to measure high-resolution PFI-ZEKE photoelectron spectra consisted of nine pulses, a first positive discrimination pulse of either 33.2 mV cm^{-1}, 83.0 mV cm^{-1}, or 166.1 mV cm^{-1} followed by eight negative extraction pulses of −83.0 mV cm^{-1}, −132.8 mV cm^{-1}, −166.1 mV cm^{-1}, −199.3 mV cm^{-1}, −232.5 mV cm^{-1}, −265.7 mV cm^{-1}, −298.9 mV cm^{-1}, and −332.1 mV cm^{-1}. The electrons generated by the field ionization of high Rydberg states induced by these negative field pulses were monitored using a microchannel-plate detector. Temporal gates were set at the positions of the electron time-of-flight spectrum corresponding to electrons produced and extracted by the individual pulses so that each laser scan led to the obtaining of eight photoelectron spectra. The positions of the ionization threshold were determined by adding the wave numbers of the two lasers used in the $(1_{VUV} + 1')$ excitation sequence and by correcting for the shift of the ionization thresholds induced by the individual field pulses, as described in Ref. 36. The absolute accuracy of the calibration procedure was better than 0.3 cm^{-1}, and the relative positions of the ionization thresholds could be determined with a precision of better than 0.02 cm^{-1} limited by the full width at half maximum in the range 0.15-0.3 cm^{-1} of individual transitions and their signal-to-noise ratio. The $(1+1')$ photoionization spectra were obtained by extracting the ions using a pulsed electric field of 330V/cm and detecting them at the end of a linear time-of-flight tube as described in Ref. 25. The ArXe dimers were formed in a pulsed, skimmed supersonic expansion of a 10:1 gas mixture of Ar:Xe using a commercial pulsed valve (General Valve, Series 9) operated at a nozzle stagnation pressure of 2.5 bar. The timing of the nozzle opening with respect to the laser pulses was set so as to optimize the formation of dimers and, at the same time, minimize the formation of higher clusters.

Figures 4 and 5 illustrate how full rovibrational and isotopomer selectivity was achieved in the intermediate level using the D-X and C-X transitions, respectively. The spectra displayed in these figures were recorded by monitoring the ion signals as a function of the wave number of the VUV laser at a fixed wave number of the ionization laser, as described in Ref. 25. Each vibrational band of the D $0^+ \leftarrow$ X 0^+ transition consists of a P and an R branch. Because of the clustering of transitions near the P-branch bandheads, R-branch lines were used to obtain full isotopomer and rotational selectivity. As illustration, the three vertical dashed lines in Figure 4 indicate the positions at which the $J' = 7$, 10, and 13 levels of the D 0^+ ($v' = 1$) level of the $^{40}Ar^{129}Xe$ isotopomer were selected. The positions of these vertical lines indeed correspond to single rovibrational transitions of only one isotopomer.

The P-, Q-, and R-branch band structure of the C 1 $\leftarrow$ X 0^+ transitions displayed in Figure 5 leads to a higher spectral density, and full selectivity could only be reached, in this case, using R-branch lines with $J'' > 7$. The dashed vertical lines in this figure mark the spectral positions at which $J' = 9$, 10, 11, and 12 *e*-symmetry levels of the C 1 ($v' = 5$) intermediate state of $^{40}Ar^{132}Xe$ were selected. Unfortunately, *f*-symmetry levels of the C state could not be cleanly selected because predissociation prevents their observation beyond $J' = 10$.[25]

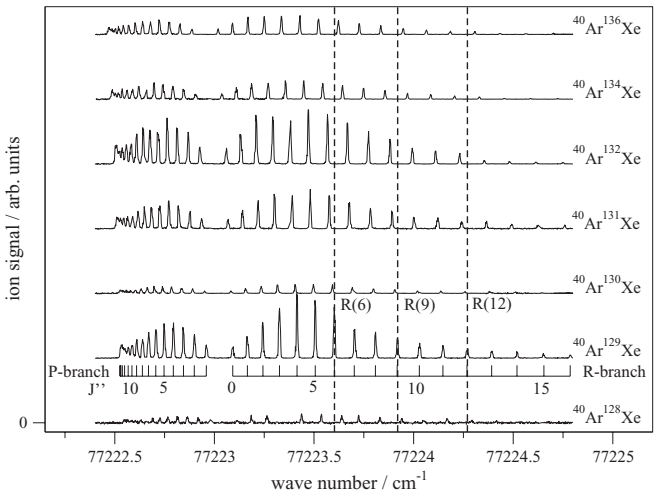

FIG. 4. REMPI spectrum of the D 0^+ ($v' = 1$) $\leftarrow$ X 0^+ ($v = 0$) transition of selected isotopomers of ArXe. The dashed vertical lines indicate the spectral positions used to selectively excite the $J' = 7$, 10 and 13 levels of the D 0^+ ($v' = 1$) state of the $^{40}Ar^{129}Xe$ isotopomer. At these positions there is overlap with transitions of only one isotopomer.

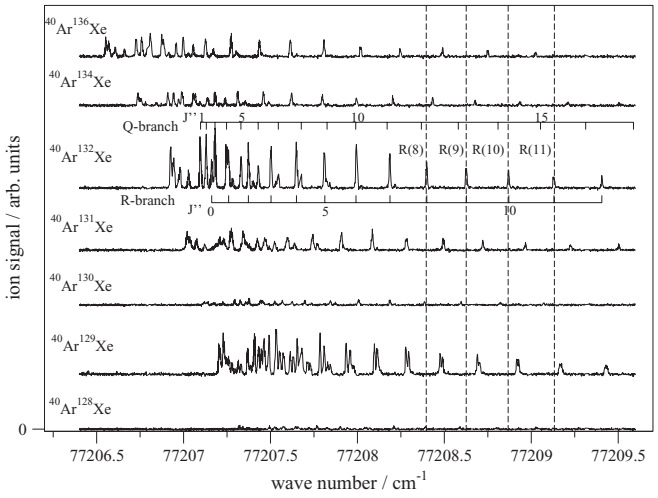

FIG. 5. REMPI spectrum of the C 1 ($v' = 5$) ← X 0^+ ($v = 0$) transition of selected isotopomers of ArXe. The dashed vertical lines indicate the spectral positions used to selectively excite the $J' = 9$, 10, 11 and 12 e-symmetry levels of the C 1 ($v' = 5$) state of the $^{40}Ar^{132}Xe$ isotopomer. At these positions there is overlap with transitions of only one isotopomer.

IV. RESULTS

Rotationally resolved spectra of the X 1/2 $v^+ = 0 - 15$, A_1 3/2 $v^+ = 0 - 3$, and A_2 1/2 $v^+ = 0 - 2, 4 - 6$ and 8 states of $ArXe^+$ could be recorded from selected rovibrational levels of the C 1 and D 0^+ states, primarily the C 1 ($v' = 5$, $J' = 9$, 11, 12, 14, 17, 20, and 23) and the D 0^+ ($v' = 1$, $J' = 7$, 10, 12, 13, 14, and 16) levels. The assignment and interpretation of the photoelectron spectra turned out to be more challenging than in the case of Ar_2^+ (Ref. 26) and Xe_2^+ (Ref. 27) for two main reasons: First, neither the spin-rotation splittings nor the Λ (Ω) doublings could be observed in any of the spectra of $ArXe^+$ whereas they could readily be observed in Ar_2^+ and Xe_2^+. Observing such splittings would have helped to overcome the ambiguities resulting, in the absence of a priori knowledge, from the four possible spectral patterns depicted in Figures 2 and 3 for the X 1/2 and A_2 1/2 states, respectively. Second, the absence of a center of symmetry in ArXe renders the simultaneous occurrence, for each transition, of even-l and odd-l photoelectron partial waves possible. The selection rules (Eq. (8)) can therefore no longer be used to deduce the parity of the ionic levels from the parity of the selected intermediate state with absolute certainty.

To try and overcome these ambiguities, it was necessary to systematically compare spectra of the same ionic states recorded through rovibronic levels of both positive and negative parity of both the C 1 and D 0^+ intermediate states and to exploit the propensity rules summarized in Table I. Whereas unambiguous rotational assignments were in the end possible for the A_1 3/2 and A_2 1/2 states, which can be efficiently accessed by direct ionization from both the C 1 and D 0^+ states, some uncertainty remained concerning the assignment of the X 1/2 ← C and X 1/2 ← D transitions, the intensity of which is dominated by rovibronic channel interactions.

An overview of spectral patterns observed for all three ionic levels (X 1/2, A_1 3/2, and A_2 1/2) from selected levels of both the C 1 and D 0^+ intermediate states is presented in Figures 6–10. In these figures, the experimental spectra are presented as inverted traces and are compared to spectra calculated on the basis of simplifying assumptions. The intensity distributions were calculated using expressions (Eqs. (9)–(11)) for the rotational line intensities derived in Refs. 31 and 32 and the orbital approximation introduced in Ref. 31 (see also Ref. 33)

$$\sigma_{\text{tot}} = \text{const} \sum_{l_o=\lambda}^{\infty} \frac{1}{2l_o + 1} Q(l_o) a_{l_o} \tag{9}$$

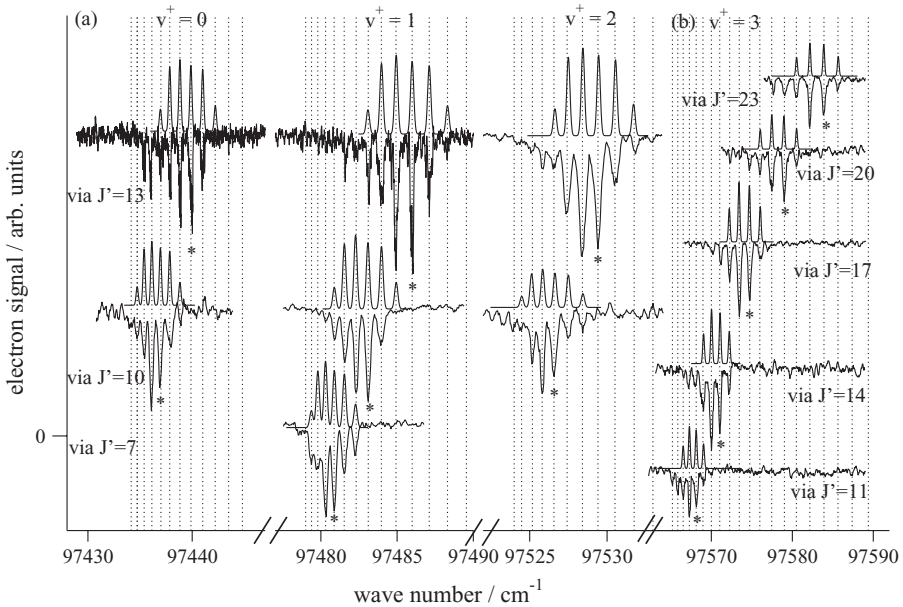

FIG. 6. Rotationally resolved PFI-ZEKE photoelectron spectra of the A_1 3/2 ($v^+ = 0$, 1, 2) levels of $^{40}Ar^{129}Xe$ (panel (a), recorded via the D 0^+ $v' = 1$ intermediate state), and of the A_1 3/2 ($v^+ = 3$) level of $^{40}Ar^{131}Xe$ (panel (b), recorded via the C 1 ($v' = 5$) intermediate state). In each panel, the experimental spectra are shown as lower, inverted traces and the calculated spectra as upper traces. The dotted vertical lines indicate the positions of the rotational levels of $ArXe^+$. The lines corresponding to the $\Delta J = J^+ - J' = 0.5$ transitions are marked with asterisks.

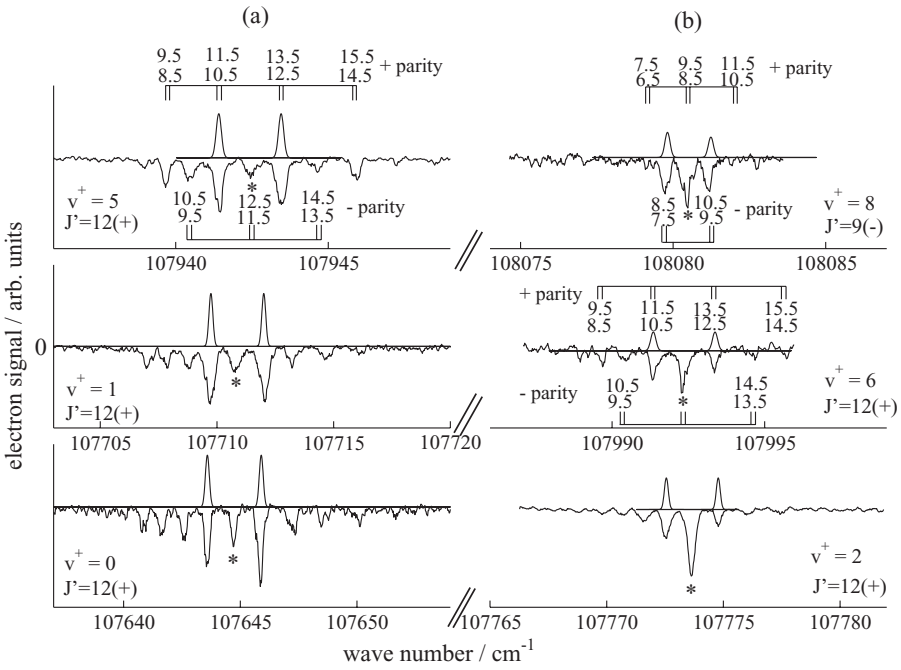

FIG. 7. Rotationally resolved PFI-ZEKE photoelectron spectra of the A_2 1/2 state of $^{40}Ar^{132}Xe$. (a) Rotational structures of the $v^+ = 0$, 1, and 5 vibrational levels recorded via the D 0^+ ($v' = 1$,$J' = 12$ (+)) intermediate state. (b) PFI-ZEKE photoelectron spectra of the A_2 1/2 ($v^+ = 2$, 6) vibrational levels recorded via the C 1 ($v' = 5$, $J' = 12$ (+)) intermediate state and of the A_2 1/2 ($v^+ = 8$) level recorded via the C 1 ($v' = 5$, $J' = 9$ (−)) intermediate state. The experimental spectra are shown as lower, inverted traces and the spectra calculated on the basis of propensity rules are depicted as upper traces (see text for details). The asterisks mark rotational lines that correspond to the overlapping $\Delta J = J^+ - J' = -0.5$ and $\Delta J = (J^+ + 1) - J' = 0.5$ transitions.

with

$$Q(l_o) = (2N^+ + 1)\begin{pmatrix} N^+ & l_o & J' \\ -\Lambda^+ & -\lambda & \Lambda' \end{pmatrix}^2 \qquad (10)$$

for transitions to the X 1/2 state, and

$$Q(l_o) = \frac{(2J^+ + 1)}{(2S^+ + 1)} \sum_{\chi} (2\chi + 1) \begin{pmatrix} l_o & S^+ & \chi \\ -\lambda & \Sigma^+ & \Lambda' - \Omega^+ \end{pmatrix}^2$$

$$\begin{pmatrix} J^+ & \chi & N' \\ -\Omega^+ & \Omega^+ - \Lambda' & \Lambda' \end{pmatrix}^2 \text{ with } \chi = l_o \pm \frac{1}{2} \qquad (11)$$

for transitions to the A_1 3/2 and A_2 1/2 states. In these equations N^+, J^+, Λ^+, S^+, Ω^+, J', and Λ' have their usual meaning. The integer value of λ is unambiguously defined by the Wigner 3j-symbol,[32] and l_o represents the dominant orbital angular momentum character of the orbital from which the electron is ejected. The orbital angular momentum quantum number l of the photoelectron partial wave is therefore equal to $l_o = \pm 1$ for a single-photon ionization process. We chose $l_o = 0$ and 1, respectively, for photoionization out of the 6s and 6p components of the wavefunctions of the C and D states, according to Table I. Clearly, this procedure cannot be expected to accurately reproduce the experimental observations but was used solely to identify and assign the most intense lines observed experimentally. The calculated spectra presented in Figures 6–10 must therefore not be regarded as illustrating agreement between state-of-the-art photoionization

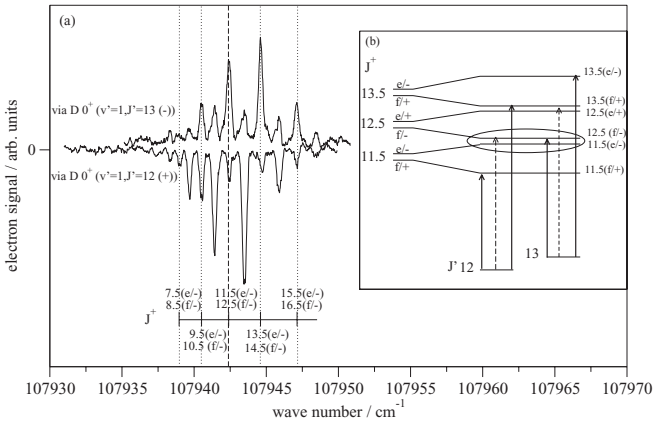

FIG. 8. (a) Rotationally resolved PFI-ZEKE photoelectron spectra of the $v^+ = 5$ vibrational level of the A_2 1/2 state of $^{40}Ar^{132}Xe$ recorded via the D 0^+ ($v' = 1$, $J' = 12(+)$ and $13(-)$) intermediate states. (b) A schematic excitation scheme from the $J' = 12(+)$, $13(-)$ intermediate levels to the overlapping Ω-doubling components of the $J^+(e)$ and $(J^+ + 1)(f)$ levels. The left-hand side of panel (b) corresponds to the case characterized by $p \approx 0$ for which each J^+ rotational level of the A_2 1/2 state consists of two closely spaced levels of opposite parity. The right-hand side of panel (b) corresponds to the case $p \approx -2B$ for which the rotational levels of the A_2 1/2 state consist of closely spaced levels of the same parity. It is only for this second case that the experimentally observed intensity alternation can be explained using the parity selection rule (Eq. (8)) in combination with a dominant $l = 1$ partial wave expected following photoionization from the $6s\sigma[A_2\ 1/2]$ component of the D 0^+ level. The bold and dotted arrows indicate intense and weak transitions observed experimentally (see panel a)), respectively. The transitions from the intermediate $J' = 12$, 13 rotational levels to the $J^+ = 11.5(e/-)$, $12.5(f/-)$ final levels are marked by the dashed line in panel (a) and correspond to the transitions indicated by the ellipse in panel (b).

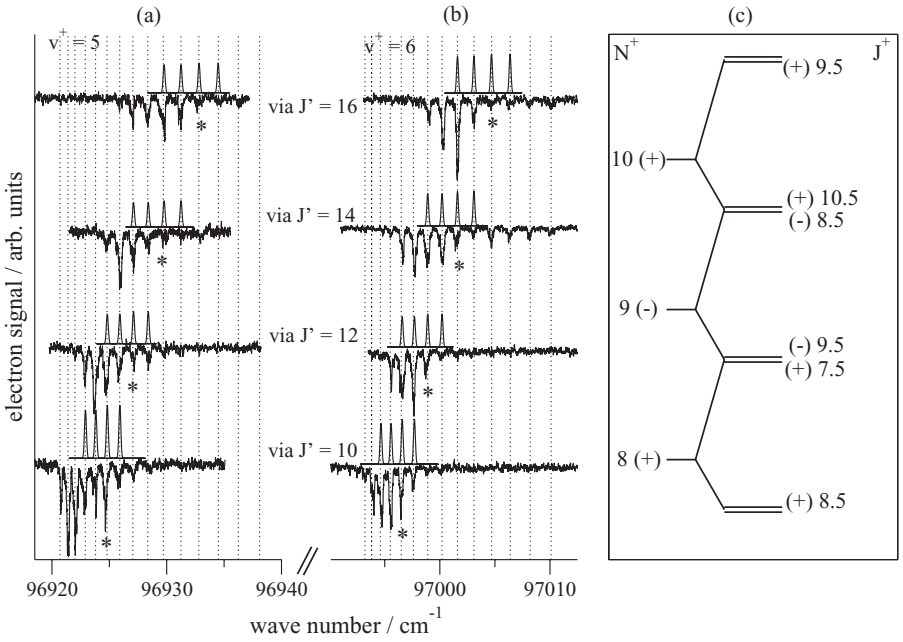

FIG. 9. Rotationally resolved PFI-ZEKE photoelectron spectra of the $v^+ = 5$ (a) and 6 (b) vibrational levels of the X 1/2 state of $^{40}Ar^{129}Xe$ recorded via the D 0^+ ($v' = 1$, $J' = 10$, 12, 14, 16) intermediate states. The lines corresponding to the overlapping $\Delta J = J^+ - J' = -0.5$ (where $J^+ = N^+ - 1/2$) and $\Delta J = J^+ - J' = 1.5$ (where $J^+ = (N^+ + 1) + 1/2$) transitions are marked with asterisks. (c) Schematic rotational energy level diagram of the X 1/2 state of $ArXe^+$.

theory and experiment but are presented here to explain our assignment procedure.

A. The A_1 3/2 ← C 1 transition

The spectra of the A_1 3/2 ($v^+ = 3$) ← C 1 ($v' = 5$) transitions displayed in Figure 6(b) were recorded after selection of the $J' = 11$, 14, 17, 20, and 23 rotational levels of the $^{40}Ar^{132}Xe$ isotopomer. This particular band of the A_1 3/2 ← C 1 band system was selected because it has the strongest intensity (see Figure 4 of Ref. 9). The A_1 3/2 state is not affected by $^2\Pi$-$^2\Sigma^+$ interaction, because it has $\Omega = 3/2$. Consequently, its rotational structure corresponds to that of a $^2\Pi_{3/2}$ state for which the Λ doubling is negligible at our resolution. Each rotational level consists of a pair of two states of same (half-integer) J value but opposite parity. The lines marked

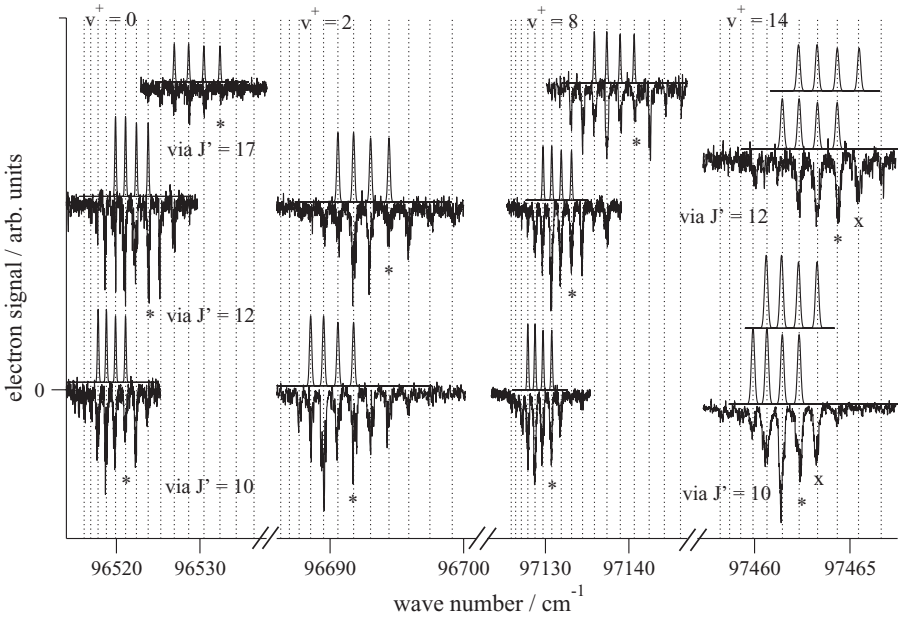

FIG. 10. Rotationally resolved PFI-ZEKE photoelectron spectra of the $v^+ = 0$, 2, 8, and 14 vibrational levels of the X 1/2 state of $^{40}Ar^{132}Xe$ recorded via the C 1 ($v' = 5$, $J' = 10$, 12, 17) intermediate levels. In each panel, the experimental spectra are shown as lower, inverted traces and the calculated spectra as upper traces. The second, upper calculated spectra presented for $v^+ = 14$ correspond to the second possible rotational assignment discussed in the text. The lines corresponding to the overlapping $\Delta J = J^+ - J' = 0.5$ (with $J^+ = N^+ - 1/2$) and $\Delta J = J^+ - J' = 2.5$ (with $J^+ = (N^+ + 1) + 1/2$) transitions are marked with an asterisk below the spectra (the cross marks the same transitions for the second possible assignment).

TABLE II. Vibronic term values $T_{3/2}^{v^+}$ and rotational constants $B_{3/2}^{v^+}$ of the A_1 3/2 state of $^{40}Ar^{129}Xe^+$, $^{40}Ar^{131}Xe^+$, and $^{40}Ar^{132}Xe^+$ determined from the rotational analysis in Hund's coupling case (a).

		$^{40}Ar^{129}Xe$		$^{40}Ar^{131}Xe$		$^{40}Ar^{132}Xe$	
State	v^+	$T_{3/2}^{v^+}$ [a]	$B_{3/2}^{v^+}$ [b]	$T_{3/2}^{v^+}$ [a]	$B_{3/2}^{v^+}$ [b]	$T_{3/2}^{v^+}$ [a]	$B_{3/2}^{v^+}$ [b]
A_1 3/2	0	97432.31(25)	0.03900(60)	...	...	...	...
	1	97478.49(16)	0.03866(60)	...	...	...	...
	2	97522.15(19)	0.03764(60)	...	...	...	...
	3	...	...	97562.95(15)	0.03648(48)	97562.83(13)	0.03625(42)

[a]Relative uncertainties. The absolute uncertainties in the wave number calibration and the determination of the electric-field-induced shift of the ionization energies are estimated to be 0.3 cm^{-1}.
[b]The Λ-doubling constant is assumed to be zero for all $^2\Pi_{3/2}$ rotational levels.

with asterisks in Figure 6(b) correspond to transitions with $\Delta J = J^+ - J' = +1/2$. The propensity rules summarized in Table I imply that (i) the electron is ejected from the [A_1 3/2] $6p\sigma$ component of the C 1 state, and (ii) the dominant rotational transitions should be characterized by Eq. (11) for $l_o = 1$, which results in $\Delta J = J^+ - J' = \pm 1/2, \pm 3/2$, and dominant $l = 0, 2$ photoelectron partial waves. The parity selection rule (Eq. (7)) further implies that the positive (negative) parity component of the Λ doublet is accessed from intermediate levels of odd (even) J' value. The calculated spectra in Figure 6(b) were obtained on the basis of these arguments. The calculations account for the four most intense lines of the experimental spectra, but do not explain the weaker lines corresponding to $\Delta J = -5/2$ and $-7/2$ that are also observed experimentally, nor for the stronger intensities of the lines corresponding to negative ΔJ values compared to those corresponding to positive ΔJ values. This asymmetry is characteristic of rotational channel interactions mediated by the electric dipole and quadrupole moments of the ion core, as explained in detail in Ref. 35. Such interactions are often observed in PFI-ZEKE photoelectron spectra of strong photoionizing transitions.

B. The A_1 3/2 ← D 0^+ transition

The spectral patterns observed for the A_1 3/2 ($v^+ = 0 - 2$) ← D 0^+ ($v' = 1$) transitions displayed in Figure 6(a) correspond closely to those observed for the A_1 3/2 ← C 1 transition with the main differences that the intensity of the $\Delta J = 3/2$ transition is stronger and that a weak $\Delta J = 5/2$ transition is observable in some spectra. The propensity rules presented in Table I predict dominant $\Delta J = \pm 1/2$ and $\pm 3/2$ photoionizing transitions. To account for the weak observed $\Delta J = +5/2$ transitions one needs to go beyond the orbital approximation and use l instead of l_o in Eq. (11). The D 0^+ state possesses $6p\pi$[A_1 3/2] character so that the overall intensity results from two contributions, one with $l = 0$ in Eq. (11) resulting in $\Delta J = \pm 1/2$ transitions and one with $l = 2$ resulting in $\Delta J = \pm 1/2, \pm 3/2, \pm 5/2$ transitions between rotational levels of opposite parity. The calculated spectra represent a sum of both contributions with equal weights and provide an explanation for the most intense transitions of each spectrum. The asymmetry favoring transitions with negative ΔJ values is consistent with the observations made in the analysis of the A_1 3/2 ← C 1 transition. The vibronic term values $T_{3/2}^{v^+}$ and rotational constants $B_{3/2}^{v^+}$ of the A_1 3/2 state determined for $^{40}Ar^{129}Xe^+$, $^{40}Ar^{131}Xe^+$, and $^{40}Ar^{132}Xe^+$ are listed in Table II.

C. The A_2 1/2 ← C 1 and D 0^+ transitions

The spectra of the A_2 1/2 ($v^+ = 0, 1$ and 5) ← D 0^+ ($v' = 1$, $J' = 12$ (+)) transitions displayed in Figure 7(a) reveal a striking intensity alternation and two dominant lines surrounding a weak central line. Our attempts at accounting for this behavior assuming a small Λ-doubling constant ($p \ll B$) corresponding to patterns (i) and (ii) of Figure 3 remained unsuccessful. Table I suggests that the dominant transitions are from the [A_2 1/2] $6s\sigma$ component of the D 0^+ state so that the dominant transitions should connect states of the same (i.e., positive) parity with $\Delta J = \pm 1/2$. The alternation of intensity then implies that the ionic rotational levels occur in pairs of levels of the same parity and therefore must correspond to patterns (iii) or (iv) in Figure 3. Of these two patterns, only pattern (iv), i.e., $p < 0$ and $|p| \approx 2B$, is compatible with the observed alternation of intensities, as illustrated by the energy level diagram drawn schematically on top of Figure 7. The spectra calculated assuming a $\Delta J = \pm 1/2$ selection rule account for the two main lines of the experimental spectra (see Fig. 7(a)). The presence of the weaker transitions to states of negative parity indicates that the $6s\sigma$ orbital must be polarized along the internuclear axis and gain $l_o = 1$ character so that photoelectron partial waves with even l character also contribute to the photoionization. To confirm this interpretation, a spectrum of the A_2 1/2 ($v^+ = 5$) ← D 0^+ ($v' = 1$) transition was recorded from the $J' = 13$ level of the D 0^+ state which has negative parity. The spectra recorded via the $J' = 12(+)$ and $J' = 13(-)$ levels are compared in Figure 8. Both spectra reveal an alternating intensity distribution with the strong and weak sets of lines interchanged. This comparison proves that the absolute value of the Λ doubling parameter p is close to $2B$ and strongly suggests that p is negative.

The C 1 ($v' = 5$) level has a [A_2 1/2]$6s\sigma$ contribution, from which one would also expect a dominant $l = 1$ photoelectron partial wave for the A_2 1/2 ← C 1 transition and therefore photoionizing transitions connecting rotational levels of the same parity. The A_2 1/2 ($v^+ = 2, 6, 8$) ← C 1 ($v' = 5$) transitions depicted in Figure 7(b) consist of three dominant lines. While the outer two lines connect rotational

TABLE III. Vibronic term values $T_{1/2}^{v^+}$ and rotational constants $B_{1/2}^{v^+}$ of the A_2 1/2 state of $^{40}Ar^{129}Xe^+$ and $^{40}Ar^{132}Xe^+$ determined from the rotational analysis in Hund's coupling case (a).

		$^{40}Ar^{129}Xe$		$^{40}Ar^{132}Xe$	
State	v^+	$T_{1/2}^{v^+}$ [a]	$B_{1/2}^{v^+}$ [b]	$T_{1/2}^{v^+}$ [a]	$B_{1/2}^{v^+}$ [b]
A_2 1/2	0	107637.43(12)	0.04624(96)	107637.49(17)	0.04619(116)
	1	107703.95(16)	0.04499(122)	107703.76(24)	0.04532(150)
	2	...	...	107766.68(15)	0.04449(79)
	3	...	...	...	...
	4	107883.46(54)	0.04199(256)	...	...
	5	107936.57(26)	0.04195(161)	107936.02(11)	0.04086(63)
	6	...	...	107986.02(27)	0.04046(165)
	7	...	...	...	...
	8	...	...	108077.12(19)	0.03743(237)

[a]Relative uncertainties. The absolute uncertainties in the wave number calibration and the determination of the electric-field-induced shift of the ionization energies are estimated to be 0.3 cm^{-1}.
[b]Assuming $p = -2B$ (see text for details).

levels of the same parity, the central most intense lines observed in these spectra are from the $J' = 12(+)$ level to the $J^+ = 11.5$ and 12.5 ionic levels of negative parity (lower two panels of Fig. 7(b)) and from the $J' = 9(-)$ to the $J^+ = 8.5$ and 9.5 ionic levels of positive parity (upper panel). These transitions, which correspond to even-l partial waves according to Eq. (8), are not predicted by our model calculations based on the propensities summarized in Table I. Possible explanations for this discrepancy are (i) that a stronger admixture of $l_o = 1$ character is induced in the C 1 state than in the D 0^+ state, or (ii) that the transitions connecting rotational levels of opposite parity originate from ionization out of the [X 1/2]6$p\sigma$ component of the C 1 state. Indeed, the [X 1/2] core consists of the same $\Omega = 1/2$ $(\pi^*)^4(\sigma^*)^1$ and $(\pi^*)^3(\sigma^*)^2$ configurations as the A_2 1/2 state. An alternative interpretation of the intensity distributions observed in Figures 7 and 8 as arising from pattern (iii) of Figure 3 cannot be entirely ruled out and would imply that it is the ionization out of the D 0^+ state rather than out of the C 1 state, that is subject to the stronger effects of l or l_o mixing. The reasons why we consider this alternative interpretation less likely are presented in Sec. V B.

The molecular constants determined for the A_2 1/2 state of $^{40}Ar^{129}Xe^+$ and $^{40}Ar^{132}Xe^+$ are summarized in Table III.

D. The X 1/2 ← C 1 and D 0^+ transitions

The rotational structures of the X 1/2 ($v^+ = 5, 6$) ← D 0^+ ($v' = 1$) and X 1/2 ($v^+ = 0, 2, 8, 12$) ← C 1 ($v' = 5$) transitions are depicted in Figures 9 and 10, respectively. Compared to the rotational structures of the A_1 3/2, A_2 1/2 ← C 1, D 0^+ band systems presented in Subsections IV A–IV C, the rotational structures of the X 1/2 ← C 1 and X 1/2 ← D 0^+ band systems are much less regular: First, the rotational intensity distribution of the same vibrational band, but recorded through different rotational levels, can be very different, as can be seen, for instance, by comparing the spectra of the $v^+ = 0$ and 8 states recorded from the $J' = 10$, 12 and 17 levels of the C 1 ($v' = 5$) state in Figure 10. Second, the rotational structure of the transitions recorded from a given intermediate level to different vibrational levels of the X 1/2 state can be very different, as is the case for transitions from the D 0^+ ($v' = 1$, $J' = 14$) to the X 1/2 ($v^+ = 5$ and 6) states in Figure 9. Third, the rotational intensity distributions of the different bands do not reveal the smooth variation with J^+ observed in the transitions to the A_1 3/2 state, nor the intensity alternations characteristic of transitions to the A_2 1/2 state. Finally, the model calculations assuming that ionization takes place out of the weak 6p components of the D 0^+ and C 1 states fail, in general, to predict the most intense transitions.

These observations are in accord with the general predictions of Table I that the direct ionization to the X 1/2 state from the C 1 and D 0^+ state is weak and that the intensities observed in the PFI-ZEKE photoelectron spectra arise from interactions with the stronger A_1 3/2 and A_2 1/2 channels. Accidental coincidences between low-lying Rydberg states belonging to series converging on the rovibrational levels of the A_1 3/2 and A_2 1/2 ionic states and the pseudo-continuum of high Rydberg states detected in PFI-ZEKE photoelectron spectra of the X 1/2 state can indeed lead to strong perturbations of the rotational intensity distributions. The photoionization spectra recorded from selected vibrational levels of the C 1 and D 0^+ state[9] provide independent evidence for the autoionization of Rydberg series converging on the A_1 3/2 and A_2 1/2 states into the continua above the X 1/2 ionization thresholds.

The irregular rotational intensity distributions of the X 1/2 ← C, D transitions rendered an unambiguous assignment of the rotational structure impossible. Careful inspection of the spectra presented in Figures 9 and 10 nevertheless enabled us to restrict possible assignments to only two. Having not observed an intensity alternation in any of the spectra, we conclude that the rotational levels of the X 1/2 state are grouped in pairs of levels of opposite parity, as illustrated in panel (c) of Figure 9. The reason why we prefer the level structure corresponding to pattern (iv) over that corresponding to pattern (iii) will be discussed in Subsection V B. Considering the intensity distributions of all bands and the fact that electronic autoionization is equally likely to enhance the intensity of transitions with positive and negative ΔJ values enables us to conclude

TABLE IV. Vibronic term values $T_{\Lambda=0}^{v^+}$ and rotational constants $B_{\Lambda=0}^{v^+}$ of the X 1/2 state of $^{40}Ar^{129}Xe^+$ and $^{40}Ar^{132}Xe^+$ determined from the rotational analysis in Hund's coupling case (b).

		$^{40}Ar^{129}Xe$			$^{40}Ar^{132}Xe$		
State	v^+	$T_{\Lambda=0}^{v^+}$ [a,b,c]	$B_{\Lambda=0}^{v^+}$ [c]	$B_{\Lambda=0}^{v^+}$ [d]	$T_{\Lambda=0}^{v^+}$ [a,b,c]	$B_{\Lambda=0}^{v^+}$ [c]	$B_{\Lambda=0}^{v^+}$ [d]
X 1/2	0	...	...	...	96513.58(6)	0.05214(35)	0.05698(38)
	1	...	...	...	96600.45(8)	0.05099(51)	0.05556(56)
	2	...	...	...	96684.41(14)	0.05103(68)	0.05521(74)
	3	...	...	...	...	...	...
	4	...	...	...	96843.25(14)	0.04850(107)	0.05324(118)
	5	96919.06(10)	0.04760(84)	0.05266(93)	...	...	...
	6	96990.75(12)	0.04825(68)	0.05235(74)	...	...	...
	7	...		...	...	...	...
	8	...	...	...	97124.21(8)	0.04549(44)	0.04933(48)
	9	...	...	...	...	...	...
	10	...	...	...	...	...	...
	11	...	...	...	97303.57(9)	0.04258(44)	0.04599(47)
	12	...	...	...	...	...	...
	13	...	...	...	97408.61(13)	0.04008(68)	0.04341(74)
	14	97458.2[e]	...	...	97456.81(11)	0.03837(77)	0.04236(85)
	15	...	...	...	97501.88(47)	0.03815(264)	0.04125(286)

[a]Relative uncertainties. The absolute uncertainties in the wave number calibration and the determination of the electric-field-induced shift of the ionization energies are estimated to be 0.3 cm^{-1}.
[b]The band origins determined for the rotational assignment corresponding to footnote d lie ~0.5 cm^{-1} higher.
[c]Assuming $\gamma^{v^+} = -2B$ (see text for details) and the assignment corresponding to the calculated spectra presented immediately above the experimental spectra in Figures 9 and 10.
[d]Assuming $\gamma^{v^+} = -2B$ (see text for details) and the assignment corresponding to the calculated spectra presented only above the X 1/2 $v^+ = 14$ spectra in Figure 10.
[e]The vibrational band intensity was insufficient for an analysis of the rotational structure.

that the two most likely assignments are the one indicated in the calculations presented immediately above the experimental spectra and the one presented only for the $v^+ = 14$ level in Figure 10.

Table IV lists the molecular constants $T_{\Lambda=0}^{v^+}$ and $B_{\Lambda=0}^{v^+}$ determined for these two possible rotational assignments of the X 1/2 state of $^{40}Ar^{129}Xe^+$ and $^{40}Ar^{132}Xe^+$.

V. DISCUSSION AND CONCLUSIONS

A. Molecular constants and potential-energy curves of the X 1/2, A_1 3/2, A_2 1/2 states of $ArXe^+$

The adiabatic ionization energies corresponding to the formation of the lowest levels of the X 1/2, A_1 3/2, and A_2 1/2 states of $ArXe^+$ from the lowest level of the X 0^+ state of ArXe, the dissociation energies of these three cationic states, their vibrational and rotational constants, and their equilibrium internuclear separations are summarized in Table V where they are compared with earlier results.

The ionization energies and the vibrational constants are overall in excellent agreement with previous experimental results. Our new values of the equilibrium internuclear separations and dissociation energies agree within the error bars with those of the potential-energy functions determined in Ref. 9. It was therefore not necessary to determine an improved set of potential-energy functions for the low-lying electronic states of $ArXe^+$ using the new high-resolution spectroscopic data presented in this article.

In a recent publication, Viehland *et al.*[21] noted the discrepancy between the dissociation energies they calculated *ab initio* with the values determined from experimental data and questioned the validity of the experimental data. While our new experimental values of the equilibrium internuclear separation and vibrational constants agree closely with the *ab initio* values reported in Ref. 21, the discrepancies in the dissociation energies are substantial. The calculations presented in Ref. 21 were based on a single-reference approximation which may have limited their accuracy. Indeed, the charge-exchange interaction was found to be significant in the analysis presented in Ref. 9.

B. Λ doubling and spin-rotation splittings

The analysis of the rotational intensity distributions of the spectra of the A_2 1/2 state indicates that the rotational level structure of this state corresponds to pattern (iv) of Figure 3, which implies that the Λ-doubling parameter p is approximately equal to $-2B$. This situation corresponds to a strong $^2\Sigma^+ - {}^2\Pi$ interaction mediated by the spin-orbit interaction[29,37,38] and makes the A_2 1/2 state look like a $^2\Sigma$ state in Hund's case (b) coupling with a small spin-rotation splitting.

The X 1/2 state appears to follow pattern (iv) of Figure 2 which implies that the spin-rotation coupling constant γ is also approximately equal to $-2B$. The X 1/2 state thus shows the behavior complementary to that of the A_2 1/2 state: Its rotational structure looks like that of a $^2\Pi$ state with almost degenerate Λ doublets.

The situation $p = \gamma$ encountered in the X 1/2 and A_2 1/2 states of $ArXe^+$ is known in the literature as being characteristic of two states in a single-perturber relationship (see the excellent discussions of this situation in Chapters 3.5 and 5.5 of Ref. 29 and in Ref. 39).

TABLE V. Adiabatic ionization energies E_i, dissociation energies D_0^+, vibrational ω_e^+ and anharmonicity $\omega_e x_e^+$ constants, equilibrium rotational constants B_e^+, vibration-rotation coupling constant α_e^+, and the equilibrium internuclear separation R_e^+ of the lowest three electronic states of $ArXe^+$. All values are in cm^{-1}, except the internuclear distance which is given in Å.

State	E_i / (hc)	D_0^+	ω_e^+	$\omega_e x_e^+$	B_e^+	α_e^+	R_e^+	Reference
X 1/2	96513.8(3)	1437.0(15)	89.74(9)	1.492(5)	0.0527(3)	$9.1(4)\cdot 10^{-4}$	3.23(1)	This work[a,b]
	96514.3(3)	1436.5(15)	89.74(9)	1.493(5)	0.0575(3)	$1.00(4)\cdot 10^{-3}$	3.09(1)	This work[a,b]
	96515.6(13)	1435.5(14)	89.34(38)	1.463(20)			3.154[c]	9[d]
							3.164[c]	
		1377.4	88.3	1.56			3.10	21[a]
	96517(2)	1432(8)	88.14(47)	1.46(2)				20[d]
		1446	89.64	1.494				6[d]
	96666(137)	1129(161)						18[d]
A_1 3/2	97432.3(3)	518.5(15)	48.89(60)	1.33(14)	0.0395(19)	$7(1)\cdot 10^{-4}$	3.74(12)	This work[e]
	97432.6(6)	518.5(7)	48.79(76)	1.30(13)			3.711[c]	9[d]
							3.721[c]	
		495.4	47.4	1.30			3.75	21[a]
	97433(3)	516(9)	50.54(160)	1.61(26)				20[d]
		548	48.49	1.267				6[d]
A_2 1/2	107637.5(3)	850.2(15)	69.24(14)	1.59(2)	0.0470(9)	$1.09(19)\cdot 10^{-3}$	3.41(4)	This work[a]
	107638.3(16)	849.7(17)	69.08(87)	1.568(79)			3.451[c]	9[d]
							3.462[c]	
		711.5	60.6	1.48			3.53	21[a]
	107636(6)	850(12)	68.39(216)	1.49(19)				20[d]
		875	69.41	1.621				6[d]

[a]Molecular constants determined for the $^{40}Ar^{132}Xe$ isotopomer.
[b]The two sets of constants arise from the two rotational assignments proposed for the X 1/2 state (see text).
[c]The two R_e values obtained in the work of Ref. 9 result from the use of two different sets of experimental data in the least-squares fit of the potential parameters.
[d]Molecular constants corresponding to a natural mixture of the isotopomers of ArXe.
[e]Molecular constants determined for the $^{40}Ar^{129}Xe$ isotopomer.

In many occurrences of the single-perturber situation, the two interacting levels are two vibrational levels, one belonging to the $^2\Sigma^+$ state and the other to the $^2\Pi_{1/2}$ state, that are accidentally almost degenerate and thus far removed from other vibrational levels of these states.

The situation encountered in $ArXe^+$ differs from this situation because the spin-orbit coupling matrix element is much larger than the vibrational spacings in the coupled $^2\Sigma^+ - {}^2\Pi$ states and even much larger than the binding energies of these two states (see Fig. 1). The "single"-perturber situation thus affects all vibrational levels of the two coupled electronic states equally and corresponds to a single "electronic" perturber situation. Under these conditions, γ_{v_Σ} of a given vibrational level of the $^2\Sigma^+$ state can be approximated by

$$\gamma_{v_\Sigma} \cong \frac{2a_+ bB_{v_\Sigma}}{\left(E_\Pi^{el} - E_\Sigma^{el}\right)/hc}. \tag{12}$$

Cohen and Schneider[40] have established that, for the rare-gas dimer ions, a_+ can be approximated by $\sqrt{2}a$, where a is the atomic value of the spin-orbit coupling constant, i.e., $-7024.617\ cm^{-1}$ (Ref. 41) for Xe^+. This approximation can be regarded as being equivalent to treating the coupled $^2\Sigma^+$ and $^2\Pi$ states arising from the $(np)^5(\sigma)^2(\pi)^4(\pi^*)^4(\sigma^*)^1$ and $(\sigma)^2(\pi)^4(\pi^*)^3(\sigma^*)^2$ configurations in Van Vleck's pure-precession approximation[37,42] for $l = 1$, in which case $a_+ = \sqrt{2}a$ and $b = \sqrt{2}$.

The separation between the $^2\Pi$ and $^2\Sigma^+$ states in $ArXe^+$ is approximately $11000\ cm^{-1}$ (see Figure 1). Under these conditions, one can estimate the values of $\gamma(=p)$ to be approximately $-2.3B$ which, considering the crude nature of the estimate, can be regarded as being in agreement with the results of our spectroscopic analysis, and justifies our preference of pattern (iv) over pattern (iii) for the rotational structure of the X 1/2 state in Figure 2, and pattern (iv) over pattern (iii) for the rotational structure of the A_2 1/2 state in Figure 3. When determining the molecular constants presented in Tables II–IV, we have therefore assumed that $\gamma = p = -2B$. We note that a similar situation has been observed by Dabrowski *et al.* in studies of the $X\ ^2\Sigma^+_{1/2}$ and $A_2\ ^2\Pi_{1/2}$ states of $HeAr^+$.[5] In Ref. 5, however, γ and p were reported to have opposite signs (i.e., $p = -\gamma = -2B$), a conclusion that was later rectified by Carrington and Softley[43] and Holland *et al.*[8]

Because A is much larger than the dissociation energy of either $\Omega = 1/2$ state, the Hund's case (c) quantum number J_a (J_a = 3/2 and 1/2 for the X 1/2 and A_2 1/2 states, respectively) is approximately a good quantum number. Under these conditions, the spin-rotation splitting and Ω doubling in the coupled $^2\Sigma - {}^2\Pi$ states are approximately described by[39,43,44]

$$-\frac{p(A_2\ 1/2)}{B} = 2(J_a + 1/2), \tag{13}$$

$$p(A_2\ 1/2) + p(X\ 1/2) = 2B, \tag{14}$$

and

$$\gamma(X\ 1/2) = 2B - p(X\ 1/2). \tag{15}$$

From these relations, one obtains $p(A_2\ 1/2) = -2B$, $p(X\ 1/2) = 4B$ and $\gamma(X\ 1/2) = -2B$, a result that is consistent with $p(X\ 1/2) = 2(J_a + 1/2)B$ for $J_a = 3/2$. Experiments at higher spectral resolution than the ones presented here would be required to provide a more stringent test of these approximations.

These arguments concerning the magnitude and sign of γ and p, when transferred to $KrXe^+$ and $NeXe^+$, would imply that the X 1/2 and A_2 1/2 states of these ions should follow the same behavior.

ACKNOWLEDGMENTS

This work is supported financially by the Swiss National Science Foundation under Project No. 200020-135342 and by the European Research Council advanced grant program under Project No. 228286.

[1]R. S. Mulliken, J. Chem. Phys. **52**, 5170 (1970).
[2]S. T. Pratt, P. M. Dehmer, and J. L. Dehmer, J. Chem. Phys. **82**, 5758 (1985).
[3]S. T. Pratt, P. M. Dehmer, and J. L. Dehmer, J. Chem. Phys. **83**, 5380 (1985).
[4]I. Dabrowski and G. Herzberg, J. Mol. Spectrosc. **73**, 183 (1978).
[5]I. Dabrowski, G. Herzberg, and K. Yoshino, J. Mol. Spectrosc. **89**, 491 (1981).
[6]K. P. Huber and R. H. Lipson, J. Mol. Spectrosc. **119**, 433 (1986).
[7]D. Hausamann and H. Morgner, Mol. Phys. **54**, 1085 (1985).
[8]F. Holland, K. P. Huber, A. R. Hoy, and R. H. Lipson, J. Mol. Spectrosc. **145**, 164 (1991).
[9]O. Zehnder and F. Merkt, J. Chem. Phys. **128**, 014306 (2008).
[10]O. Zehnder and F. Merkt, Mol. Phys. **106**, 1215 (2008).
[11]E. Kleimenov, L. Piticco, and F. Merkt, Mol. Phys. **106**, 1835 (2008).
[12]J. S. Cohen and B. Schneider, Phys. Rev. A **11**, 884 (1975).
[13]V. Aquilanti, D. Cappelletti, and F. Pirani, Chem. Phys. Lett. **271**, 216 (1997).
[14]A. Wüest and F. Merkt, J. Chem. Phys. **118**, 8807 (2003).
[15]A. Wüest and F. Merkt, Chem. Phys. Lett. **397**, 344 (2004).
[16]E. Kleimenov, O. Zehnder, and F. Merkt, J. Mol. Spectrosc. **247**, 85 (2008).
[17]L. Piticco, F. Merkt, A. A. Cholewinski, F. R. W. McCourt, and R. J. Le Roy, J. Mol. Spectrosc. **264**, 83 (2010).
[18]C. Y. Ng, P. W. Tiedemann, B. H. Mahan, and Y. T. Lee, J. Chem. Phys. **66**, 5737 (1977).
[19]H. Yoshii, T. Tanaka, Y. Morioka, T. Hayaishi, and K. Ito, J. Chem. Phys. **111**, 10595 (1999).
[20]H. Yoshii, T. Hayaishi, T. Onuma, T. Aoto, Y. Morioka, and K. Ito, J. Chem. Phys. **116**, 7468 (2002).
[21]L. A. Viehland, B. R. Gray, and T. G. Wright, Mol. Phys. **108**, 547 (2010).
[22]A. P. Hickman, D. L. Huestis, and R. P. Saxon, J. Chem. Phys. **96**, 2099 (1992).
[23]S. Liberman, J. Phys. (Paris) **30**, 53 (1969).
[24]T. Tsuchizawa, K. Yamanouchi, and S. Tsuchiya, J. Chem. Phys. **92**, 1560 (1990).
[25]L. Piticco, M. Schäfer, and F. Merkt, J. Chem. Phys. **136**, 074304 (2012).
[26]P. Rupper and F. Merkt, J. Chem. Phys. **117**, 4264 (2002).
[27]K. Vasilatou, U. Hollenstein, and F. Merkt, Mol. Phys. **108**, 915 (2010).
[28]L. Veseth, J. Phys. B **6**, 1473 (1973).
[29]H. Lefebvre-Brion and R. W. Field, *The Spectra and Dynamics of Diatomic Molecules* (Elsevier, Amsterdam, 2004).
[30]J. Xie and R. N. Zare, J. Chem. Phys. **93**, 3033 (1990).
[31]A. D. Buckingham, B. J. Orr, and J. M. Sichel, Philos. Trans. R. Soc. London, Ser. A **268**, 147 (1970).
[32]J. Xie and R. N. Zare, J. Chem. Phys. **97**, 2891 (1992).
[33]S. Willitsch and F. Merkt, Int. J. Mass Spectrom. **245**, 14 (2005).
[34]H. Park and R. N. Zare, J. Chem. Phys. **104**, 4568 (1996).
[35]F. Merkt and T. P. Softley, Int. Rev. Phys. Chem. **12**, 205 (1993).
[36]U. Hollenstein, R. Seiler, H. Schmutz, M. Andrist, and F. Merkt, J. Chem. Phys. **115**, 5461 (2001).
[37]R. S. Mulliken and A. Christy, Phys. Rev. **38**, 87 (1931).
[38]G. Herzberg, *Molecular Spectra and Molecular Structure: Spectra of Diatomic Molecules*, Vol. I, 2nd ed. (Krieger, Malabar, 1989).
[39]I. Kopp and J. T. Hougen, Can. J. Phys. **45**, 2581 (1967).
[40]J. S. Cohen and B. Schneider, J. Chem. Phys. **61**, 3230 (1974).
[41]H. J. Wörner, M. Grütter, E. Vliegen, and F. Merkt, Phys. Rev. A **71**, 052504 (2005); see erratum, **73**, 059904(E) (2006).
[42]J. H. Van Vleck, Phys. Rev. **33**, 467 (1929).
[43]A. Carrington and T. P. Softley, Chem. Phys. **92**, 199 (1985).
[44]J. T. Hougen, J. Mol. Spectrosc. **42**, 381 (1972).